ADVANCED FUNCTIONAL MATERIALS

FULL PAPER

DOI: 10.1002/adfm.200600938

Strain Accommodation during Phase Transformations in Olivine-Based Cathodes as a Materials Selection Criterion for High-Power Rechargeable Batteries**

By *Nonglak Meethong*, *Hsiao-Ying Shadow Huang*, *Scott A. Speakman*, *W. Craig Carter*, and *Yet-Ming Chiang**

High energy lithium-ion batteries have improved performance in a wide variety of mobile electronic devices. A new goal in portable power is the achievement of safe and durable high-power batteries for applications such as power tools and electric vehicles. Towards this end, olivine-based positive electrodes are amongst the most important and technologically enabling materials. While certain lithium metal phosphate olivines have been shown to be promising, not all olivines demonstrate beneficial properties. The mechanisms allowing high power in these compounds have been extensively debated. Here we show that certain high rate capability olivines are distinguished by having extended lithium nonstoichiometry (up to ca. 20 %), with which is correlated a reduced lattice misfit as the material undergoes an electrochemically driven, reversible, first-order phase transformation. The rate capability in several other intercalation oxides can also be correlated with lattice strain, and suggests that nanomechanics plays an important and previously unrecognized role in determining battery performance.

1. Introduction

Following the first journal publication describing the use of olivine compounds as rechargeable battery electrodes,[1] the potential for reduced cost and improved safety[2] of this class of materials was quickly appreciated, but, because of the lower volumetric energy compared with compounds such as $LiCoO_2$ and the poor rate capability, the practical utility was unclear. Interest in high power applications grew rapidly after Chung et al.[3] demonstrated high capacity at charge/discharge rates well above 5 C in doped nanoscale $LiFePO_4$ (e.g., 115 mA h g^{-1} for 20 C continuous discharge at room temperature[4]), but it also raised controversy over the origin of the exceptional rate performance.[5–10] The ability to obtain high power while retaining reasonably high energy, along with inherent safety and long cycle life (many thousands of charge/discharge cycles), seems likely to enable many new classes of applications. However, not all olivines have exhibited high rate capability, a notable exception being $LiMnPO_4$, which is otherwise attractive for its higher theoretical energy.[11–13] Numerous studies have attributed the rate capability of olivines purely to chemical diffusion limitations.[1,3,6–8,10–12,14] Indeed, either electronic and ionic conductivity can be rate-limiting under certain conditions. However, noting that this class of olivines undergoes a first-order phase transition upon electrochemical cycling, we reasoned that an equally important goal should be to maximize the rate of phase transformation, regardless of the rate-limiting step. Thus, we considered whether the phase transformation kinetics, which correspond directly to the rate of lithium exchange, might be affected by other, structural, factors.

2. Test Materials

We performed comparative electrochemical tests and X-ray structural analysis on two types of lithium iron phosphates. The first was a recently synthesized material, cation-doped $LiFePO_4$ prepared for earlier publications,[3,4] denoted NC. Figure 1 shows the discharge capacity versus rate behavior for a sample of similar performance to those originally described. For comparison, we used a high-surface-area "carbon-added" $LiFePO_4$ (Aldrich Chemical), denoted AC, of similar carbon content to the NC samples (Table 1). This material has a higher rate capability than untreated pure $LiFePO_4$, but its capacity at rates above 1 C is well below that of the NC sample (Fig. 1). Identical formulations, active material loadings, and preparation methods were used to prepare samples for electrochemical testing, as described in the Experimental section. It is emphasized that neither material is believed to represent the state-of-

[*] Prof. Y.-M. Chiang, N. Meethong, Dr. H.-Y. S. Huang, Prof. W. C. Carter
Department of Materials Science and Engineering
Massachusetts Institute of Technology
Cambridge, MA 02139 (USA)
E-mail: ychiang@mit.edu
Dr. S. A. Speakman
Center for Materials Science and Engineering
Massachusetts Institute of Technology
Cambridge, MA 02139 (USA)

[**] N.M. and H.-Y.S.H. contributed equally to this work. N.M. acknowledges support by the Royal Thai Government Scholarship Program. Supporting Information is available online from Wiley InterScience or from the author.

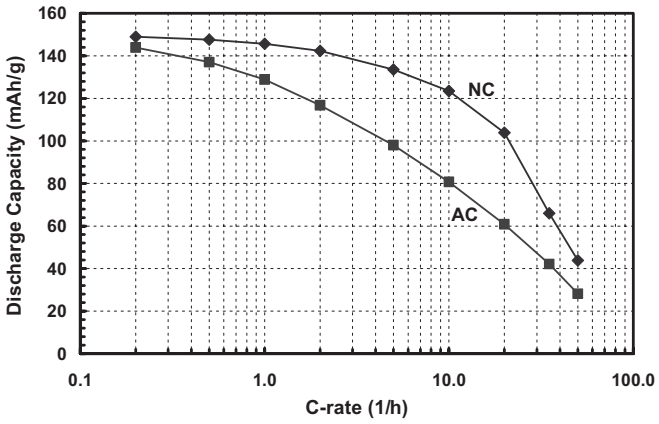

Figure 1. Comparison of specific discharge capacity versus galvanostatic C rate for samples NC (top) and AC (bottom), representing high rate capability doped nanoscale and "carbon-added" lithium iron phosphates respectively, measured in lithium half-cells of Swagelok type. Before each discharge, cells were charged at C/2 rate and held at 3.8 V until the current decays to C/25 rate.

the-art capability of any particular manufacturer, and, the samples are not selected for maximum contrast in rate capability, but because all of the experiments discussed herein were performed on them. At the time this study was initiated, sample AC was the only commercially available "battery grade" $LiFePO_4$. For NC-type samples, partial data were also available for a number of similar materials and are consistent with the results presented here.

Table 1 shows the physical and structural characteristics of the two samples along with data for olivines from several literature reports. The NC sample of $Li_{0.99}Nb_{0.01}FePO_4$ composition was prepared according to a published procedure,[3] and has a specific surface area of. 39.2 $m^2 g^{-1}$, corresponding to an equivalent spherical particle diameter of 43 nm. Sample AC has a specific surface area of 14.8 $m^2 g^{-1}$ corresponding to a 113 nm diameter, which is high compared to lithium battery cathodes such as $LiCoO_2$ and $LiMn_2O_4$ (typically <1 $m^2 g^{-1}$). Although we attempted to increase the particle size of both materials through heat treatment in order to obtain systematic size variations, significant changes were not achieved except under temperatures and gas ambients that also produced detectable amounts (by X-ray) of impurity phases, primarily metal phosphides. Nonetheless, the samples in this study can be compared with those of several previous publications, listed in Table 1, all of which are expected to have lower rate performance than either of the two sample types measured here.

It should also be noted that in the case of sample NC, a comparative study of the high rate performance of various olivines by Striebel et al.[7] included results for an Massachusetts Institute of Technology (MIT)-supplied electrode that were inferior to those described here and in the original publications;[3,4]

Table 1. Physical and structural characteristics of a high rate capability, doped nanoscale lithium iron phosphate (Sample NC) and lower-rate "carbon-added" lithium iron phosphate (Sample AC), compared with literature data for $LiFePO_4$ and $LiMnPO_4$. SOC: state-of-charge.

	Sample NC	Sample AC	Padhi [1]	Yamada [16]	Yamada [16]	Yamada [18]	Andersson [33]	Yamada [32]
Compositional state	≈ 50 % SOC	≈ 50 % SOC	Stoichiometric	Solid solution limits	Stoichiometric	Stoichiometric	Stoichiometric	Stoichiometric
Specific surface area [$m^2 g^{-1}$]	39.2	14.8	Not reported	8–15	8–15	Not reported	Not reported	Not reported
Carbon content [wt %]	2.4	1–3 [a]	Not reported	Not reported	Not reported	Not reported	Not reported	Not reported
$LiFePO_4$ phase								$LiMnPO_4$
a [Å]	10.232	10.3289	10.334	10.309	10.323	10.32287	10.329	10.46
b [Å]	5.941	6.0069	6.008	6.0010	6.0065	6.00496	6.0065	6.11
c [Å]	4.730	4.6905	4.693	4.6980	4.6930	4.69094	4.6908	4.75
V [$Å^3$]	287.502	291.0224	291.392	290.64	290.99	290.784	291.02	303.58
Strain [%]	0.66	0.02						
Crystallite size [Å]	266	1145.4						
$FePO_4$ Phase								$MnPO_4$
a [Å]	9.887	9.8267	9.821	9.8290	9.8170	9.81465	9.8142	9.64
b [Å]	5.838	5.7944	5.792	5.7995	5.7900	5.7887	5.7893	5.92
c [Å]	4.7786	4.7832	4.788	4.7793	4.7822	4.78107	4.782	4.773
V [$Å^3$]	275.824	272.3572	272.357	272.44	272.82	271.632	271.7	272.39
Strain [%]	0.355	0.05						
Crystallite size [Å]	276.3	799.6						
Misfit [%] [b]								
Linear strain								
a axis	3.430	4.983	5.091	4.767	5.025	5.047	5.111	8.159
b axis	1.749	3.601	3.661	3.415	3.671	3.667	3.683	3.159
c axis	–1.022	–1.957	–2.004	–1.716	–1.883	–1.903	–1.926	–0.483
Volume strain	4.146	6.626	6.753	6.464	6.445	6.811	6.867	10.830
Planar strain								
ab plane	5.178	8.581	8.747	8.179	8.691	8.711	8.790	11.311
ac plane	2.408	3.027	3.087	3.052	3.143	3.145	3.187	7.677
bc plane	0.727	1.645	1.657	1.700	1.788	1.765	1.757	2.676

[a] Quoted by manufacturer. [b] Taken as the difference/mean value.

ADVANCED FUNCTIONAL MATERIALS

namely, only ca. 100 mA h g^{-1} at 10 C rate. There may be a simple explanation for this discrepancy—Striebel et al. comment that a large additional impedance was necessary to model the electrode provided,[7] which suggests that delamination of the electrode coating from the current collector had occurred. In our measurements, samples of the same type retained up to 85 mA h g^{-1} capacity (50 % of the theoretical value) at 50 C rate at room temperature. Applied in larger-scale cells, similar materials used in cylindrical lithium ion cells of 26 mm diameter and 65 mm length provide ca. 3 kW kg^{-1} power density and ca. 110 W h kg^{-1} energy density.[15]

3. Electrochemical Measurements

Galvanostatic charging and discharging measurements were first performed using lithium half-cells (Fig. 2). For each sample, only a small difference in polarization was seen between C/50 and C/100 rate measurements, indicating that kinetic limitations were negligible at these slow rates (Fig. 2). The voltage–capacity curves show deviations from the two-phase plateau voltage at the beginning and end of charge that suggest a compositionally narrower two-phase field for the NC materials, Figure 2. The plateau voltage is slightly higher for the NC sample. This is not due to greater polarization, but instead, due to a difference in the open-circuit voltage (OCV) of about 0.006 V between the two materials (confirmed by repeat measurements), which reflects a thermodynamic difference. Although the polarization of these cells was small, suggesting that the observed voltages are close to equilibrium values, sloping voltage curves at low and high states of charge in galvanostatic measurements are commonly attributed to kinetic limitations. Therefore, we sought a measurement that could provide definitive measurements of the extent of equilibrium nonstoichiometry.

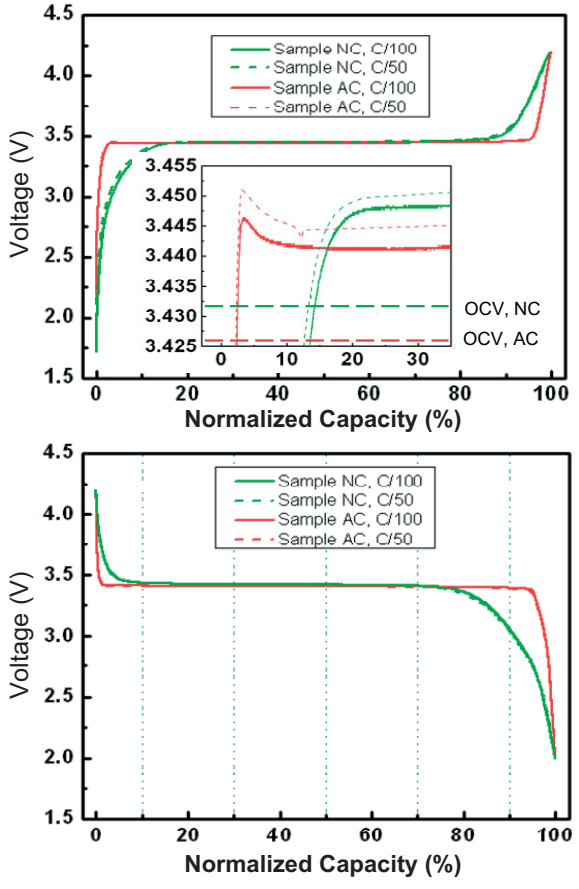

Figure 2. Galvanostatic charging (top) and discharge (bottom) at C/50 and C/100 rates shows the narrower composition range over which high rate capability, doped nanoscale powders (sample NC) exhibit a constant cell voltage indicating two-phase coexistence, compared to the lower rate capability carbon-added sample AC. Note also the overpotential measured on charge for sample AC as the two-phase plateau voltage is approached, absent for sample NC (inset). The open-circuit voltage (OCV) differs slightly for the two samples as discussed in text and indicated in the inset.

Galvanostatic intermittent titration tests (GITT), in which voltage relaxation after the application of current pulses is measured, is often used to establish the thermodynamic voltage versus composition. However, when a first-order phase transition is present, current pulsing inherently leads to an increase in the overpotential, which could introduce hysteresis effects when nucleation of the new phase or migration of the phase boundary occurs. (GITT was nonetheless performed on some NC samples and gave results consistent with those presented here.)

Instead, a potentiostatic intermittent titration test (PITT) was used in which the capacity was measured at small voltage increments progressing through the open-circuit voltage (OCV) of the cell (Fig. 3). After each voltage step, the current decay (to a C/50 rate or less) provided the charge or discharge capacity available at that voltage. The OCV was first measured to ±2 mV precision with the cells at 50 % lithiation, a composition that is well within the two-phase field. PITT was then conducted starting from the discharged or charged states, approaching the two-phase voltage in 5 or 10 mV steps. By conducting the measurement in this manner, no thermodynamic driving force is applied for the phase transformation during charging until the open-circuit voltage (OCV) corresponding to two-phase coexistence is exceeded. Thus, any charge capacity accumulated below the OCV can be attributed to states available to lithium ions before the new phase is nucleated; that is, it is due to the formation of a lithium-excess solid solution, starting with a delithiated material. Similarly, upon discharge from a higher voltage, there is no driving force for the phase transition until the applied voltage falls below the OCV (we will refer to both instances as the imposition of an "overpotential"). Here, any charge capacity accumulated above the OCV voltage can be attributed to the formation of a lithium excess solid solution in the lithiated starting material. We use x to denote lithium deficiency in the lithium-rich end-member (e.g., $Li_{1-x}FePO_4$ and $Li_{0.99-x}Nb_{0.01}FePO_4$) and y to denote lithium excess in the lithium-poor end-member (e.g., Li_yFePO_4 and $Li_yNb_{0.01}FePO_4$). The results of the PITT measurements are plotted in Figure 3 in a manner resembling cyclic voltammograms (CV) except that the vertical axis is capacity and not current.

Sample NC (Fig. 3a) exhibits substantial capacity upon both charging and discharging before the two-phase OCV is

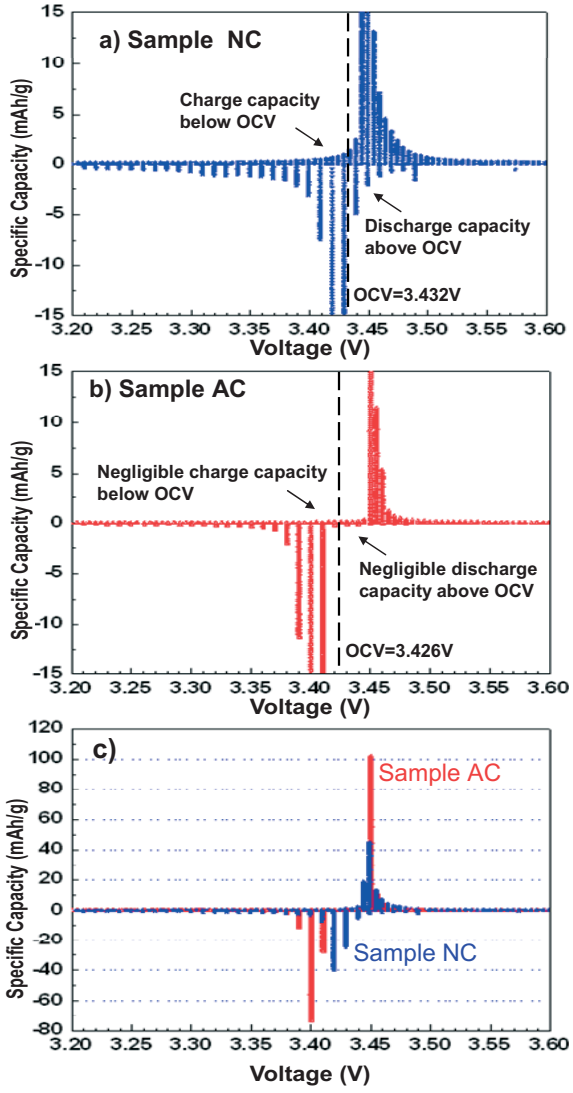

Figure 3. Capacity versus voltage measured potentiostatically upon charge and discharge in 10 mV steps. The OCV is indicated for each cell. a) Nb-doped nanoscale sample NC; b) carbon-added undoped $LiFePO_4$ sample AC. c) Full-scale representation of the data.

reached, while sample AC (Fig. 3b) exhibits virtually no capacity upon either charge or discharge until an overpotential of ca. 30 mV is applied. The maximum extent of solid-solution nonstoichiometry, x and y, measured with the last voltage increments being within 10 mV of the OCV, is 19.6 % and 11.7 %, respectively, for sample NC, and 1.4 % and 1.0 %, respectively, for sample AC. Results for sample AC are consistent with previous findings[1,9,16,17] of very limited lithium nonstoichiometry in both end-members near room temperature. (A recent neutron diffraction study does suggest somewhat higher stoichiometry than that derived from lattice constants.)[18] Chung et al.[3] proposed that the improved properties of their doped nanoscale materials resulted from extended lithium solid solubility not achievable in conventional $LiFePO_4$. The present electrochemical measurements as well as the structural data presented below support their original interpretation.

4. Diffraction Studies

We determined whether the excess nonstoichiometry measured electrochemically is a surface or bulk effect. It is possible that in a high-surface-area powder, excess nonstoichiometry can arise from surface sites differing in Li chemical potential from bulk intercalation sites. Surface chemical activity can also lead to the formation of space charge surface layers[19] penetrating into the crystal, although the high defect concentration of the present materials implies a very compact (sub-nanometer) space charge width. To distinguish nonstoichiometry occurring at the surface alone from that occurring within the volume of the particles, we carried out powder X-ray diffraction on samples that were electrochemically cycled to 50 % state-of-charge (SOC). The coexistence of the lithiated and delithiated phases means that each is at its maximum limit of mutual solid solubility (maximum nonstoichiometry) at the test temperature. The electrochemically cycled cells were allowed to rest for more than 24 h before being disassembled and analyzed by X-ray diffraction (Fig. 4). The X-ray diffraction results showed that the lattice parameters of the coexisting phases vary in accordance with the electrochemically determined nonstoichiometry, indicating that bulk effects must be considered. Reitveld refinement provided lattice parameters for the coexisting lithium-rich and lithium-poor phases, as well as the crystallite strain and crystallite size of each phase.

As shown in Table 1, the X-ray crystallite sizes for samples NC and AC are in good agreement with those deduced from their specific surface areas. In each case the delithiated phase has the smaller unit cell volume, with smaller a and b parameters and a larger c parameter. For sample AC, the absolute values of the lattice parameters and the unit cell volume are in good agreement with literature (Table 1). However, in sample NC, the unit cell volumes of the lithiated and delithiated phases are lower and higher, respectively, consistent with the lithium nonstoichiometry measured electrochemically. Applying Vegard's law to the unit cell volume and using the lattice constants reported in the literature,[16] the nonstoichiometry in sample NC is $x = 19.5\,\%$ and $y = 16.5\,\%$, while the nonstoichiometry in sample AC is nominally zero since the unit cell volumes of the triphylite and heterosite phases are slightly larger and smaller respectively than the literature data, Table 1.

Extended lithium nonstoichiometry is therefore inferred in the NC samples from three independent tests: low-rate galvanostatic tests (Fig. 1), PITT tests (Fig. 2), and lattice parameter measurements (Table 1). Note that the galvanostatic and PITT measurements approach the phase boundary from a limiting solid solution that is either fully lithiated or fully delithiated, and thus measures the maximum nonstoichiometry that can be obtained without requiring nucleation of the other phase. In contrast, the structural measurements are performed on samples that approach equilibrium from a two-phase coexistence, namely, from within the two-phase field. The good agreement between these measurements indicates that the nonstoichiometry is a true, equilibrium feature of the phase diagram for the NC samples and that the primary cause of the lattice parameter variations is indeed lithium nonstoichiometry. How the doping

ADVANCED FUNCTIONAL MATERIALS

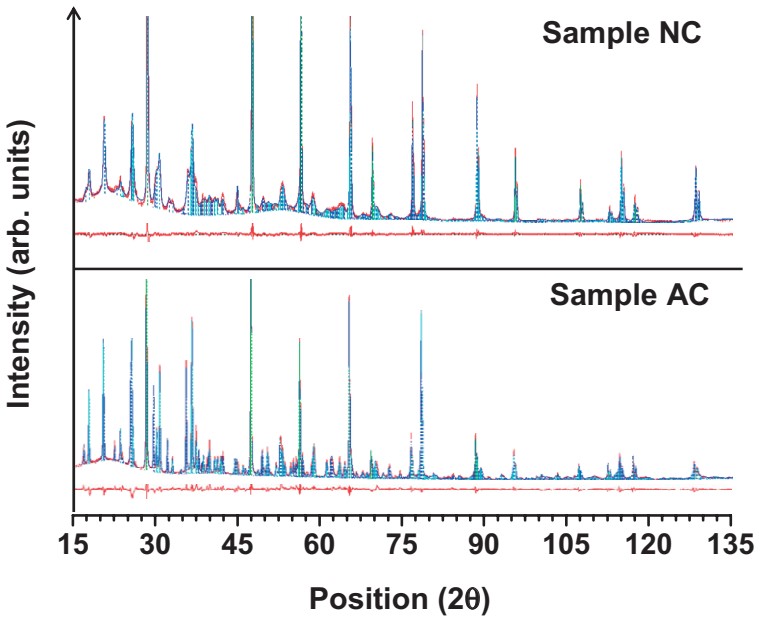

Figure 4. Rietveld refined X-ray patterns for samples NC and AC at ca. 50% state of charge, including the fit to Si powder added as an internal standard. The observed intensity data are shown by the solid red line, and the dashed blue, aqua, and green lines overlying them are the calculated intensity of $LiFePO_4$, $FePO_4$, and Si, respectively. The dashed lines are the calculated intensity of the aluminum peaks from the current collector. The difference between the observed and calculated intensities is shown for each of the pattern. The structural results are shown in Table 1.

combined with nanoscale particle size in the NC samples stabilizes such large nonstoichiometry is not completely clear, but we note that the small heat of demixing in the $LiFePO_4/FePO_4$ system (ca. 600 J mol^{-1})[17] implies sensitivity of the phase stability to small changes in composition and introduced defects. A related study[20] of undoped nanoscale $LiFePO_4$ has shown that the miscibility gap shrinks systematically as the particle size decreases, demonstrating clearly the existence of a size-dependent nonstoichiometry. However, at equivalent size (ca. 40 nm) the extent of solid solution is only about one-half of that measured in sample NC. Regardless of the origin, the availability of such large nonstoichiometry within both solid-solution phases, corresponding to coexistence of Fe^{2+} and Fe^{3+}, suggests that the electronic structure and transport properties will differ from those of the pure end-member phases ($LiFePO_4$ and $FePO_4$) considered in most studies to date.

5. Coupling between Elastic Misfit, Lithium Nonstoichiometry, and Rate Capability

In correlation with the extended nonstoichiometry (increased mutual solid solubility) is a large decrease in the lattice misfit between the lithiated and delithiated phases. The percentage misfit between the lithiated and delithiated phases for the *a*, *b*, and *c* parameters, the unit cell volume (*abc*), and the unit cell faces *ab*, *ac*, and *bc* are given in Table 1. There is significantly lower lattice misfit in the high rate NC sample compared to all others. The volume misfit in sample AC is 6.63%, within the range 6.45–6.87% published for $LiFePO_4$, whereas in sample NC it is reduced by one third to 4.15%. Even more striking is the difference in misfit between the principal crystal planes. Given the relatively isotropic elastic constants of $LiFePO_4$,[21] from purely elastic considerations, we expect the interface between coexisting phases to form preferentially on the plane of minimum strain, which is the *bc* or {100} plane. Chen et al.[22] have recently observed that cycled $LiFePO_4$ cracks along the {100} plane, consistent with this expectation. Equally important, their observations show that the misfit in conventional $LiFePO_4$ is large enough, even along the plane of minimum strain, to cause rupture. The fracture plane appears to be dominated by these simple elastic considerations, even though faster lithium diffusion along the *b* axis might be expected to produce a preference for growth of the *ac* plane ({010} plane). For sample AC as well as the literature data, the strain in this plane is 1.65–1.79%. By contrast, in the high rate sample NC, the strain is reduced to 0.73%, which, as we show, should allow the interface to remain coherent and permit facile phase propagation with reduced accumulated elastic or plastic strains.

The PITT tests also provided a direct measurement of each sample's transformation rate as a function of overpotential. During two-phase coexistence, and assuming no capacitive current, no short circuits, or other regions of lithium accumulation, the current measured in PITT is exactly linear to the phase transformation rate. The PITT data showed completely different kinetics in the two types of samples (Fig. 5). Firstly, a smaller overpotential (ca. 15 mV) is required to propagate the first-order phase transition in sample NC compared with sample AC (ca. 30 mV). The NC sample shows a maximum current at the start of each voltage increment, followed by rapid but monotonic decay. Significantly, sample AC shows a completely different response in which the current is initially low, rising slowly to reach its maximum value ca. 4 h later. This kinetic response clearly cannot be modeled by any "simple" diffusional process, and suggests a phase transformation barrier that is gradually overcome at constant potential as the phase transformation proceeds. Similar results were obtained upon discharge, and after multiple cycles.

The amount of retained crystallographic strain in the partially transformed materials further shows that these materials can be distinguished on the basis of elastic misfit. The formation of a coherent interface implies that the adjoining crystals, if misfitting, have been strained in order to maintain the coherence. On the other hand, the formation of an incoherent interface implicitly relaxes lattice strain. These effects are well-known for other phase transformations and in the growth of epitaxial thin films. Because of the high elastic moduli of inorganic compounds, percent-level differences in strain can have enormous impact on failure and coherency (the strain to failure of ceramic crystals is typically much less than 1%). Even in very thin films, less than ca. 1% lattice strain is typically required in order to obtain a coherent interface.[23] Sample NC, despite having a low-

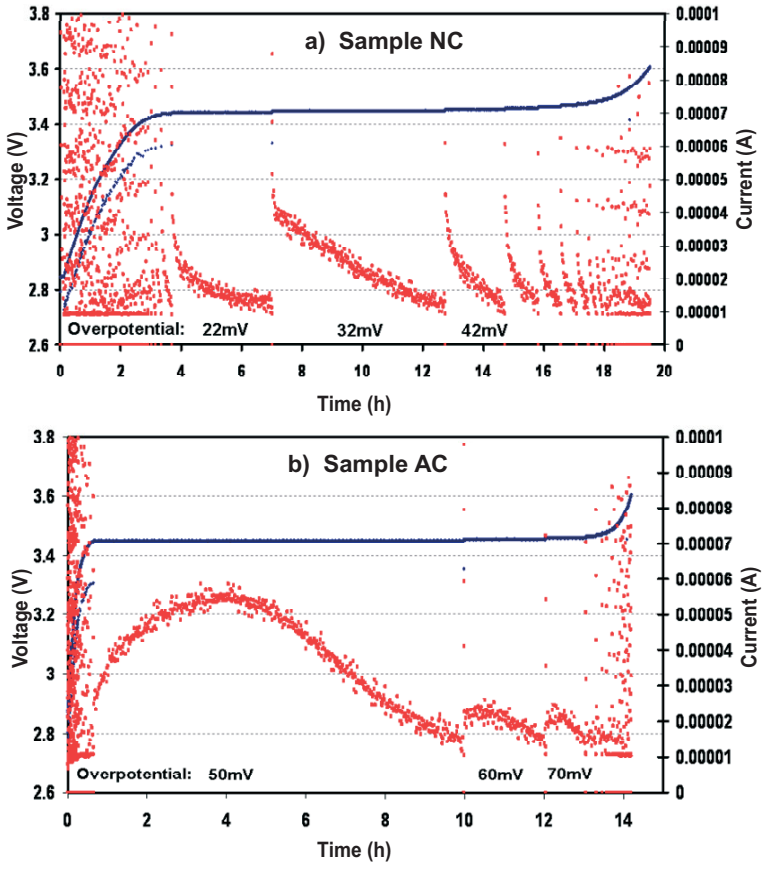

Figure 5. Voltage steps (black) and corresponding current relaxation (red) during PITT measurements (10 mV steps, C/50 current cutoff) in the second charge cycle, indicating rate of phase transformation as a function of the applied potential. a) The doped nanoscale sample NC exhibits peak current at the start of each voltage step followed by monotonically decaying current at all overpotentials. b) The comparison sample AC exhibits a slow increase in the current at constant voltage, peaking nearly 4 h after the application of overpotential, indicating a time-varying barrier to phase transformation. Higher overpotentials are also required for phase transformation.

er lattice misfit than sample AC, nonetheless shows higher retained strain in both the triphylite and heterosite phases, 0.66 % and 0.36 %, respectively (Table 1). This suggests that if coherency is producing the retained strain, the misfit has not been relieved. Sample AC, by contrast, has negligible retained crystallographic strain (0.02 % and 0.05 %). This would be consistent with the formation of incoherent, strain-relieving interfaces. However, an alternative explanation for the retained strain is a variation in lithium stoichiometry due to a distribution of particle sizes. Although particles within a composite electrode such as those used here are expected to rapidly come to equilibrium with one another, the Gibbs–Thomson effect dictates that their individual compositions may vary. The importance of this effect can be evaluated once the particle size distributions are known.

6. Thermodynamic Model

Stored elastic energy may therefore contribute to the thermodynamics of two-phase reactions. While electrochemically induced volume changes leading to fracture of storage materials have been widely postulated as a cause of capacity loss and poor cycle life (these strains have also recently been used to advantage for mechanical actuation[24,25]), to our knowledge the thermodynamic effects of mechanical strain energy have not been treated. Interfacial energy terms may also be important in opposing or promoting phase transformation, especially in nanoscale materials. The following nucleation theory for strained intercalation compounds takes these contributions into account. Although the principles apply to any intercalation compound that undergoes a volume change with composition (i.e., the ions occupy interstitial sites), including materials cycled predominantly within a solid-solution field such as $LiCoO_2$ and $LiMn_2O_4$, for simplicity we consider compounds that undergo a first-order phase transition, a class that includes the olivines, $Li_4Ti_5O_{12}$,[26] and the "lithiated spinel" $Li_2Mn_2O_4$.[27]

The molar free energy versus lithium concentration at fixed temperature for two coexisting bulk phases in the absence of elastic energy is depicted in Figure 6a. Considering a positive electrode and a negative electrode of constant lithium chemical potential (e.g., lithium metal), the cell voltage is $\Delta\mu_{Li} = \phi^+ - \phi^-$, the difference in chemical potential is $\Delta\mu_{Li} = \mu^+_{Li} - \mu^-_{Li}$, and at equilibrium the two are related by $ZF\Delta\phi = -\Delta\mu_{Li}$ if there are no other effects accompanying the production of a second phase such as those considered below. Electroneutrality requires Zn_e moles of electrons to be transferred for n_{Li} moles of the ion; $Z = 1$ for lithium. The tangent to the free energy curve intersects the right vertical axis (representing one mole of lithium transported at chemical potential μ^+_{Li}) at a value $-F\Delta\phi(x)$ that gives the equilibrium cell voltage. The cell voltage $\Delta\phi(x)$ decreases with increasing lithium concentration for compositions in the left single-phase field up to $x = x^1$, has a constant value for compositions in the two-phase field between x^1 and x^2, and decreases again within the right single-phase field for $x > x^1$.

Now consider the formation of a new phase with lattice distortion compared to the pre-existing phase. If the interface between the two phases does not permit sliding (i.e., a perfectly coherent interface) or the geometry of the two phases within the particle prohibits sliding (e.g., a spherical shell surrounding a sphere of one phase), then the stored elastic energy raises the system's potential energy. Considering reversible isothermal changes in the system's potential energy, it can be shown that two-phase equilibrium occurs when

$$FZ\Delta\phi = \Delta\mu_{Li} + \frac{V_M^I}{C}\frac{du_{elstc}}{dV_f} \quad (1)$$

where V_f is the volume fraction of phase 2 in a total volume V_T of electrode material, C is the number of lithium atoms to con-

ADVANCED FUNCTIONAL MATERIALS

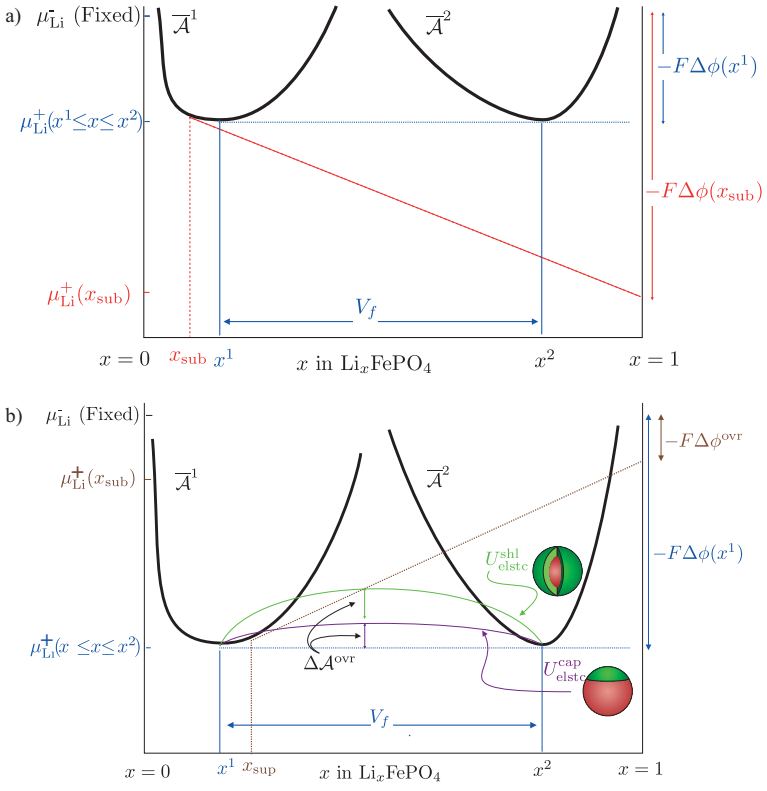

Figure 6. a) Molar free energy of two positive electrode phases illustrating tangent construction relating chemical potential differences and electromotive force in the absence of stored elastic energy. The reference energies are scaled so that the common tangent has zero slope. b) Within the two-phase region, a coherent interface between phases differing in molar volume produces an additional contribution to the molar free energy and is illustrated for the case of a spherical shell and spherical cap.

vert phase 1 to phase 2, V_M^I is the molar volume of initial phase 1, and u_{elstc} is the elastic energy per volume V_T.

A "core/shell" model[1] whereby the newly formed phase uniformly coats the pre-existing phase has been widely adopted to explain the behavior of olivines. Approximating the electrode material as spherical particles, the new phase would form a spherical shell, in which case u_{elstc} can be calculated exactly and directly from the equations of isotropic elastic equilibrium assuming identical elastic constants E (Young's modulus) and ν (Poisson's ratio) for both phases. For small $\Delta V_M/V_M^I$, this exact result for the elastic energy density is approximated by

$$u_{elstc} \approx \frac{\left(\frac{\Delta V_M}{V_{M^I}}\right)^2 E V_f (V_f - 1)}{9(1-\upsilon)} \quad (2)$$

where $\Delta V_M = V_M^{II} - V_M^I$ is the difference in molar volume.

For at least two reasons, the assumption of a shell of uniform thickness is implausible. First, there are alternative configurations of lower elastic energy. We used a finite element method to calculate u_{elstc} for a geometry consisting of a spherical cap of phase 2 with a flat coherent interface separating it from the rest of the sphere of phase 1. The calculated elastic energy is less than that of the shell (Eq. 2) by a factor of 10/3 (Supporting Information, Fig. S1). In anisotropic crystals such as the present one, the ability to choose planes of low misfit and orientations of lower elastic modulus further reduces the energy of the cap configuration. Although the computed increases to the equilibrium potential $\Delta\phi$ due to elastic energy alone are modest, on the order of tens of millivolts, the cap configuration is clearly preferred. A second reason the spherical shell geometry is not preferable derives from nucleation considerations: the first infinitesimal increment in V_f requires a finite interfacial area (the sphere area) for the spherical shell configuration but an infinitesimal interfacial area for the cap configuration.

Thus to formulate a nucleation model, we first take the major components of the volumetric energy to be the chemical and elastic energies. Referring to Figure 6b, a slightly super-saturated solid solution of the delithiated phase (e.g., Li_yFePO_4) that is stress-free has a lower equilibrium potential $\Delta\phi(x)$ than that of the equilibrium composition. When any portion of the supersaturated solution then transforms to a two-phase configuration, the molar free energy change, represented by the vertical distance ΔA^{ovr}, can be positive or negative depending on the lattice misfit, elastic constants, geometrical configuration of the initial and nucleated phases, and the magnitude of the applied overpotential. Evaluating numerically, we find that a severalfold larger overpotential is required for ΔA^{ovr} to become negative for the spherical shell than for the cap configuration. Upon adding the interfacial energy between phases 1 and 2, which is the product of interfacial tension, γ, and the interfacial area (readily written in terms of V_T and V_f for the shell and cap geometries), the driving force for the energetically-preferred spherical cap configuration is

$$\Delta A_{ptcl}^{cap}(V_f) = \Delta A^{ovr} V_T V_f + g\gamma V_f^{2/3} V_T^{2/3} \quad (3)$$

where g is a geometrical constant of order unity related to the interfacial area. Note that the first term is negative and the second positive; both include a dependence on the transformed fraction, V_f. There exists a critical V_f at which the driving force for transformation becomes negative (otherwise a solid solution is preferred), given by

$$V_f^{crit} = \frac{-8g^3\gamma^3}{27(\Delta A^{ovr})^3 V_T} \quad (4)$$

A large negative volume energy ΔA^{ovr} reduces the critical fraction while the strong sensitivity to interfacial energy, γ, indicates that a large misfit creating incoherent interfaces will increase the overpotential needed to induce transformation. The interfacial energy barrier to nucleation is minimized by having low interface tension γ, which for the present olivines is probably best satisfied by interfaces forming on the {100} plane. Although the present calculation is for spheres, this will be true

for any relatively equiaxed particle shape, as well as anisometric shapes where the smallest cross-section falls on the {100} plane.

Returning to the experimental data, in light of these considerations, for sample AC, both an abrupt overpotential seen during the continuous charging at the beginning of the two-phase voltage plateau (Fig. 1) and the unusual kinetic response at constant overpotential (Fig. 5) strongly suggest that a barrier to phase transformation must be overcome. Both features are absent in the high rate capability sample NC of lower misfit. Note that the form of the elastic energy versus volume fraction transformed (Fig. 6b and S1) is similar to the rate of phase transformation (current flow) versus extent of transformation at a constant overpotential in Fig. 5.

7. Kinetic Limitations in the Presence of Incoherent Interfaces

For sufficiently large elastic misfit, other, kinetic limitations must also be considered. We hypothesize that for large enough lattice misfit, and at a critical volume fraction, interface dislocations are nucleated and cause the interface to become incoherent. The incoherent interface should have a markedly slower migration rate. Unlike a coherent interface that can migrate due to Li transport alone, the strain-accommodating dislocations in an incoherent interface comprise discontinuities in the other atomic sublattices of the olivine structure (e.g., Fe, P, or O) and cannot be removed simply by the addition or removal of lithium. Instead, as with other such interfaces, the phase boundary may only move at a rate slow enough to allow the dislocations to be annihilated by climb and glide processes to the particle surface. This means that diffusion of an atomic species other than lithium may become rate-limiting. Under cyclic conditions, we may imagine that the transforming crystal faces the following dilemma. Either the phase transformation proceeds at a slow rate limited by dislocation migration, or additional dislocations may be generated with each pass of the interface. The first creates a rate-limiting step that is likely much slower than the chemical diffusion rate of lithium, and the second presents an additional energy barrier to the transformation, as well as accumulating damage that can eventually cause fracture of the particles. Indeed, transmission electron microscopy of sample AC after 30 high-rate charge/discharge cycles reveals a high density of dislocations, as observed in other compounds such as $LiCoO_2$.[28] Extended defects of any kind were difficult to detect in the NC particles, although additional microscopy is needed for definitive conclusions.

8. Summary and Conclusions

Extended lithium nonstoichiometry has been observed in both end-member phases of high rate doped nanoscale lithium iron phosphates, associated with which is a reduction in the lattice misfit between coexisting phases in comparison to conventional materials. In the NC sample studied here, the nonstoichiometry measured at room temperature would otherwise be attained in a conventional material only at elevated temperatures of 200–400 °C.[9,17] The coexistence of Fe^{2+} and Fe^{3+} in the solid solution, and the associated changes in lattice parameters and bond lengths of the nonstoichiometric solid solutions, should be expected to alter the electronic structure, increase electronic conductivity, and possibly influence ionic conductivity in comparison with conventional samples. As proposed previously,[3] it is likely that electronic conductivity will be improved to where it is no longer rate-limiting. Beyond altered transport coefficients, however, the elastic strain affects both thermodynamic and kinetic aspects of the phase transition. It is suggested that high-rate materials are able to retain coherent interfaces throughout nucleation and growth of the new phase, providing "facile" phase transformation. A partially transformed material may consist of two-phase particles, or may relax to an assembly in which each particle is purely one phase or the other in order to avoid the energy penalty of a retained interface. However, lithiation or delithiation of the assemblage as a whole will require nucleation and propagation of a new phase within individual particles. In olivines, reduced misfit along the {100} plane may be an important factor. This, we suggest, is as important to high rate capability as improvements in ionic and electronic transport.

Generality of the proposed model is suggested by correlations between elastic misfit and rate capability in several other lithium intercalation oxides exhibiting first-order phase transitions. The poor rate capability of $LiMnPO_4$ compared to $LiFePO_4$ has been attributed solely to its low electronic conductivity.[11,12] However, there is also a much larger misfit between the phases (ca. 10 vol %, Table 1) than in $LiFePO_4$. The fact that even nanoscale $LiMnPO_4$ has a much poorer rate capability[13] than conventional $LiFePO_4$-based materials suggests that lattice misfit plays an important role. $Li_4Ti_5O_{12}$, on the other hand, is a cubic spinel known for having nearly zero dimensional change between its lithiated and delithiated phases,[26] and is also known for having exceptional rate capability when produced in nanoscale form.[28] A third example is the spinel $LiMn_2O_4$. Between the composition limits MnO_2 and $Li_{0.5}MnO_2$, there exists a continuous solid-solution cubic spinel that is known for its high rate capability—this spinel is the basis for certain high-power lithium-ion batteries. However, upon further lithiation, a first-order phase transition from $Li_{0.5}MnO_2$ to tetragonal "$Li_2Mn_2O_4$" occurs with a 5.6 % volume misfit and 16 % change in the *c*/*a* ratio.[26,29] The rate capability in this regime is found to be markedly inferior to that of the cubic spinel.[30] We know of no counterexamples in which high rate capability is obtained for a phase transformation of large misfit. Thus, a strain-based predictive criterion for the design and selection of high power battery electrode compounds is suggested.

9. Experimental

Electrochemical tests were performed on electrodes formulated with 79 wt % positive active material, 10 wt % conductive carbon black

(Super P, M.M.M. Carbon, Belgium) and 11 wt % Kynar 2801 binder, using acetone as the solvent. The formulation was coated onto aluminum foil current collectors at a loading of ~5 mg cm^{-2} of active material, and assembled in Swagelok™ type or coin cells using Li metal foil as the counterelectrode, a microporous polymer (Celgard 2400, Hoechst Celanese Corporation, Charlotte, NC, USA) or glass fiber separator, and liquid electrolyte mixtures containing 1:1 by weight ethylene carbonate:dimethyl carbonate (EC:DMC) or ethylene carbonate:diethyl carbonate (EC:DEC), and 1 M $LiPF_6$ as the conductive salt. Arbin or Maccor instrumentation was used for the galvanostatic and potentiostatic tests. Charge/discharge rates are reported in the C-rate convention, or *C*/*n*, where *n* is the time (h) for complete charge or discharge of the nominal capacity measured at low rates. High rate discharge capacities were obtained by first charging at C/2 rate to 3.8 V and holding until the current decayed to C/25, followed by galvanostatic discharge at the desired rate to 2.0 V. For the PITT measurements, the open-circuit potential of each cell at 50 mol % lithiation (well within the two-phase field) was first measured to ±2 mV precision, then 10 mV steps were taken starting from the fully discharged or fully charged state, and the capacity measured at each voltage increment until a C/50 lower current limit was reached.

For X-ray diffraction structural analysis, the Swagelok cells were taken to 50 % state of charge, rested for >24 h, and disassembled. About 0.0005 g Si powder (Alfa Aesar, USA) was embedded in the top surface of the electrodes as a standard. X-ray patterns were obtained using a Rigaku RTP500RC instrument with a rotating anode and Cu Kα radiation, and were slow scanned at 0.15° min^{-1} over a 2θ range from 15° to 135°. The structural parameters were refined by Rietveld analysis using a PANalytical X'Pert HighScore Plus software. The Rietveld refinements gave the structural parameters in Table 1 with goodness of fit and weighted residual error parameter (GOF and R_{wp}) values of less than 4.0 and 10.0, respectively, indicating reliable refinements.

The elastic energy of spherical shell and spherical cap configurations were modeled using Ansys 8.0 (Ansys Inc., Canonsburg, PA). A thermal conduction model of the same geometry was constructed first and tested, following which the structural model was constructed by switching to an equivalent structural element. Materials properties and structural symmetry boundary conditions were specified, and the overall elastic energy was calculated for the different geometrical configurations.

Received: October 10, 2006
Published online: March 21, 2007

[1] A. K. Padhi, K. S. Najundaswamy, J. B. Goodenough, *J. Electrochem. Soc.* **1997**, *144*, 1188.

[2] A. S. Andersson, J. O. Thomas, B. Kalska, L. Häggström, *Electrochem. Solid-State Lett.* **2000**, *3*, 66.

[3] S. Y. Chung, J. T. Bloking, Y.-M. Chiang, *Nat. Mater.* **2002**, *1*, 123.

[4] S. Y. Chung, J. T. Bloking, Y.-M. Chiang, *Nat. Mater.* **2003**, *2*, 702.

[5] Ravet et al. [6] contended that the high rate capability was due to inadvertent carbon coating, despite TEM evidence to the contrary [2]. Striebel et al. [7] attributed the rate capability to particle size alone, arguing that their "core/shell" transport model could adequately model the behavior without changing the assumed chemical diffusion coefficient of lithium. Subramanya Herle et al. [10] argued that the high electronic conductivities reported by Chung et al. were due to nanoscale networks of phosphide-carbide phases, but their observations were of sintered pellets and no electrochemical measurements were reported. Delacourt et al. [8,9] have argued firstly that aliovalent doping of $LiFePO_4$ is not possible, and secondly that the process used by Chung et al. results in conductive coatings of carbon or metal phosphides on the particles, again despite high-resolution microscopy results refuting both [3]. Neither Delacourt et al. [8] nor Subramanya Herle et al. [10] provided electrochemical tests of their doped materials.

[6] N. Ravet, A. Abouimrane, M. Armand, *Nat. Mater.* **2003**, *2*, 702.

[7] K. Striebel, J. Shim, V. Srinivasan, J. Newman, *J. Electrochem. Soc.* **2005**, *152*, A664.

[8] C. Delacourt, C. Wurm, L. Laffont, F. Sauvage, J.-B. Leriche, R. Bouchet, M. Morcrette, J.-M. Tarascon, C. Masquelier, in *Proc. MRS Fall Meeting* (Eds: P. Knauth, C. Masquelier, E. Traversa, E. D. Wachsman), The Materials Research Society, Warrendale, PA **2004**, 321.

[9] C. Delacourt, P. Poizot, J.-M. Tarascon, C. Masquelier, *Nat. Mater.* **2005**, *4*, 254.

[10] P. Subramanya Herle, B. Ellis, N. Coombs, L. Nazar, *Nat. Mater.* **2004**, *3*, 147.

[11] A. Yamada, S. C. Chung, *J. Electrochem. Soc.* **2004**, *151*, A1352.

[12] C. Delacourt, L. Laffont, R. Bouchet, C. Wurm, J.-B. Leriche, M. Morcrette, J.-M. Tarascon, C. Masquelier, *J. Electrochem. Soc.* **2005**, *152*, A913.

[13] N. H. Kwon, T. Drezen, I. Exnar, I. Teerlinck, M. Isono, M. Grätzel, *Electrochem. Solid-State Lett.* **2006**, *9*, A277.

[14] V. Srinivasan, J. Newman, *J. Electrochem. Soc.* **2004**, *151*, A1517.

[15] A. Chu, *Development of HEV batteries with lithium iron phosphate cathodes*, presented at the Advanced Automotive Battery Conf., Baltimore, MD, June 2006. See also: www.A123Systems.com.

[16] A. Yamada, H. Koizumi, N. Sonoyama, R. Kanno, *Electrochem. Solid-State Lett.* **2005**, *8*, A409.

[17] J. L. Dodd, R. Yazami, B. Fultz, *Electrochem. Solid-State Lett.* **2006**, *9*, A151.

[18] A. Yamada, Y. Takei, H. Koizumi, N. Sonoyama, R. Kanno, K. Ito, M. Yonemura, T. Kamiyama, *Nat. Mater.* **2006**, *5*, 357.

[19] See for example: a) Y.-M. Chiang, A. F. Henriksen, W. D. Kingery, D. Finello, *J. Am. Ceram. Soc.* **1981**, *64*, 383. b) J. A. S. Ikeda, Y.-M. Chiang, *J. Am. Ceram. Soc.* **1993**, *76*, 2437. c) J. A. S. Ikeda, Y.-M. Chiang, A. J. Garratt-Reed, J. B. Vander Sande, *J. Am. Ceram. Soc.* **1993**, *76*, 2447.

[20] N. Meethong, H.-Y. S. Huang, W. C. Carter, Y.-M. Chiang, *Electrochem. Solid-State Lett.,* in press.

[21] T. Maxisch, G. Ceder, *Phys. Rev. B* **2006**, *73*, 174 112.

[22] G. Chen, X. Song, T. Richardson, *Electrochem. Solid-State Lett.* **2006**, *9*, A295.

[23] E. A. Fitzgerald, *Dislocations in Strained-Layer Epitaxy: Theory, Experiments, and Applications*, North-Holland, New York **1991**.

[24] Y. Koyama, T. E. Chin, U. Rhyner, R. K. Holman, S. R. Hall, Y.-M. Chiang, *Adv. Funct. Mater.* **2006**, *16*, 492.

[25] T. E. Chin, U. Rhyner, Y. Koyama, S. R. Hall, Y.-M. Chiang, *Electrochem. Solid-State Lett.* **2006**, *9*, A134.

[26] K. Ariyoshi, R. Yamato, T. Ohzuku, *Electrochim. Acta* **2005**, *51*, 1125.

[27] M. M. Thackeray, *Prog. Solid State Chem.* **1997**, *25*, 1.

[28] H. Wang, Y.-I. Jang, B. Huang, D. R. Sadoway, Y.-M. Chiang, *J. Electrochem. Soc.* **1999**, *146*, 473.

[29] L. Kavan, J. Procházka, T. M. Spitler, M. Kalbáč, M. Zukalová, T. Drezen, M. Grätzel, *J. Electrochem. Soc.* **2003**, *150*, A1000.

[30] Y.-M. Chiang, H. Wang, Y. Jang, *Chem. Mater.* **2001**, *13*, 53.

[31] N. Meethong, D.-W. Kim, Y.-M. Chiang, unpublished.

[32] A. Yamada, S.-C. Chung, *J. Electrochem. Soc.* **2001**, *148*, A960.

[33] A. S. Anderson, J. O. Thomas, *J. Power Sources* **1999**, *81*, 463.